AIAA Journal
Vol. 45, No. 4, April 2007

Role of Turbulent Prandtl Numbers on Heat Flux at Hypersonic Mach Numbers

X. Xiao,* H. A. Hassan,† and J. R. Edwards‡
North Carolina State University, Raleigh, North Carolina 27695-7910
and
R. L. Gaffney Jr.§
NASA Langley Research Center, Hampton, Virginia 23681-2199

DOI: 10.2514/1.21447

A new turbulence model suited for calculating the turbulent Prandtl number as part of the solution is presented. Because of the high Reynolds numbers involved, a formulation based on the Reynolds-averaged Navier–Stokes equations is developed. The model is based on a set of two equations: one governing the variance of the enthalpy and the other governing its dissipation rate. These equations were derived from the exact energy equation and thus take into consideration compressibility and dissipation terms. The model is used to study three cases involving shock-wave/boundary-layer interaction at Mach numbers of 9.22, 8.18, and 5.0. In general, heat transfer prediction for separated flows showed improvement over traditional turbulence models in which the turbulent Prandtl number is assumed constant. It is concluded that using a model that calculates the turbulent Prandtl number as part of the solution is a key to bridging the gap between theory and experiment for hypersonic flows dominated by strong shock-wave/boundary-layer interactions.

I. Introduction

MOST simulation of hypersonic turbulent flows involving strong shock-wave/boundary-layer interaction invariably overestimate the heat flux by almost a factor of 2 if two-equation models are used [1]. One possible reason for such performance is a result of the fact that the turbulence models employed make use of Morkovin's hypothesis [2]. This hypothesis is valid for nonhypersonic Mach numbers and moderate rates of heat transfer. At hypersonic Mach numbers, high rates of heat transfer exist in regions in which strong shock-wave/boundary-layer interactions are important. For such flows, temperature fluctuations, which are as important as velocity fluctuations at the higher Mach numbers, play a major role in determining the wall heat flux, and their effects must explicitly be taken into consideration. As a result, one should not expect traditional turbulence models to yield accurate results.

The goal of this investigation is to explore the role of a variable Prandtl number formulation in predicting heat flux in flows dominated by strong shock-wave/boundary-layer interactions. The intended applications involve flows in the absence of combustion, such as those encountered in supersonic inlets. In principle, direct numerical simulation (DNS) or large eddy simulations (LES) can be used to address this problem. LES formulations require subgrid-scale modeling and, for the closure of the heat flux vector, a constant turbulent Prandtl number is often assumed [3]. Hybrid LES/RANS approaches employ a similar closure [4]. All of these time-dependent techniques can be prohibitively expensive for high Reynolds number flows.

Because of the high Reynolds numbers involved and a need to obtain steady solutions in a cost-effective manner, an approach based on the Reynolds-averaged Navier–Stokes (RANS) equations is employed. This approach requires the solution of equations for the temperature (enthalpy) variance and its dissipation rate. Such equations can be derived from the exact Navier–Stokes equations. Traditionally, modeled equations (see, for example, [5,6]) are based on the low-speed energy equation in which the pressure gradient term and the term responsible for energy dissipation are ignored. It is clear that such assumptions are not valid for hypersonic flows. The variable turbulent Prandtl number approach developed by Brinckman et al. [7] is based on an energy equation similar to that used in [5,6]. The current approach is based on the exact energy equation and thus accounts for pressure gradient and dissipation terms.

The approach used here is based on the procedure used in deriving the k-ζ model [8], in which the exact equations that governed k, the variance of velocity, and ζ, the variance of vorticity, were derived and modeled. For the variable turbulent Prandtl number, the exact equations that govern the temperature (enthalpy) variance and its dissipation rate are derived and modeled term by term. The resulting equations are free of damping and wall functions and are coordinate-system independent. Moreover, modeled correlations are tensorially consistent and invariant under Galilean transformation.

Two flat-plate experiments are used to determine model constants. The first is the Mach (M) 9.2 experiments of Coleman and Stollery [9] that were conducted in a hypersonic gun tunnel at Imperial College. The second is the $M = 8.3$ experiments of Kussoy et al. [10] that were conducted in the NASA Ames Research Center 3.5-ft hypersonic wind tunnel facility. These turned out to be a major undertaking because of the different facilities and instrumentation and because no accuracy estimates of heat transfer measurements were provided. The model is validated by three sets of experiments. The first is the 15-deg ramp of [9] at $M = 9.22$ and $Re/L = 47 \times 10^6/\mathrm{m}$. The second is the reflected shock experiments of Kussoy and Horstman [11] and Horstman [12], conducted in the NASA Ames Research Center 3.5-ft hypersonic wind tunnel at $M = 8.18$ and $Re/L = 16 \times 10^6/\mathrm{ft}$. Both of the preceding experiments employed intrusive measurements. The third experiment is the recent nonintrusive measurements by Schülein [13] of

---

Presented as Paper 1098 at the 43rd AIAA Aerospace Sciences Meeting and Exhibit, Reno, NV, 10–13 January 2005; received 29 November 2005; revision received 19 December 2006; accepted for publication 7 January 2007.

*Research Assistant Professor, Department of Mechanical and Aerospace Engineering. Member AIAA.

†Professor, Department of Mechanical and Aerospace Engineering. Fellow AIAA.

‡Professor, Department of Mechanical and Aerospace Engineering. Associate Fellow AIAA.

§Aerospace Engineer, Hypersonic Air Breathing Propulsion Branch. Senior Member AIAA.

flows involving shock-wave/boundary-layer interactions at $M = 5$ and $Re/L = 37 \times 10^6/\mathrm{m}$. The measurements were carried out at the Ludwieg-tube facility at the DLR, German Aerospace Research Center. Oil-film interferometry techniques were used to measure skin friction, and an infrared camera system was used for heat transfer measurements.

The recent measurements of Schülein [13] were a repeat of an earlier experiment [14] that did not include heat transfer measurements or skin friction measurements in the separated flow region. Calculations of the earlier experiments were carried out by Nance and Hassan [15] using a k-ζ two-equation model and an abbreviated stress model. It was concluded in [15] that there was a need to develop turbulence models capable of predicting the turbulent Prandtl number as part of the solution.

It is shown in this study that a variable Prandtl number formulation results in significant improvement of heat transfer predictions in the presence of strong shock-wave/boundary-layer interactions that are characterized by flow separation. However, the new model has an insignificant influence on wall pressure and skin friction distributions.

II. Formulation of the Problem

A. Governing Equations

The energy equation can be written as

$$\rho\frac{\mathrm{D}h}{\mathrm{D}t} = \frac{\partial}{\partial t}(\rho h) + \frac{\partial}{\partial x_i}(\rho u_i h) = \frac{\mathrm{D}p}{\mathrm{D}t} - \frac{\partial q_i}{\partial x_i} + \phi \equiv S_h \tag{1}$$

where

$$q_i = -\lambda\frac{\partial T}{\partial x_i} \qquad \phi = t_{ij}\frac{\partial u_i}{\partial x_j} \qquad t_{ij} = 2\mu\left(S_{ij} - \frac{1}{3}\delta_{ij}\frac{\partial u_m}{\partial x_m}\right)$$
$$S_{ij} = \frac{1}{2}\left(\frac{\partial u_i}{\partial x_j} + \frac{\partial u_j}{\partial x_i}\right) \tag{2}$$

ρ is the density, h is the enthalpy, p is the pressure, u_i is the velocity, and λ and μ are the coefficients of thermal conductivity and molecular viscosity. Noting that

$$\frac{\mathrm{D}P}{\mathrm{D}t} = R\rho\frac{\mathrm{D}T}{\mathrm{D}t} + RT\frac{\mathrm{D}\rho}{\mathrm{D}t} \tag{3}$$

and using the relation $h = C_P T$ and the conservation of mass equation, Eq. (1) can be rewritten as

$$\rho\frac{\mathrm{D}h}{\mathrm{D}t} = -(\gamma - 1)\rho h\frac{\partial u_i}{\partial x_i} + \gamma\left(-\frac{\partial q_i}{\partial x_i} + \phi\right), \qquad \gamma = C_P/C_v \tag{4}$$

where C_P and C_v are the specific heats at constant pressure and constant volume.

The mean energy equation follows from Eq. (1) as

$$\frac{\partial}{\partial t}(\bar{\rho}\,\tilde{h}) + \frac{\partial}{\partial x_i}(\bar{\rho}\,\tilde{h}\,\tilde{u}_j) = \frac{D\bar{P}}{\mathrm{D}t} - \frac{\partial \bar{q}_i}{\partial x_i} + \bar{\phi} - \frac{\partial}{\partial x_j}(\bar{\rho}\,\widetilde{h''u_j''}) \tag{5}$$

where

$$\bar{\phi} = \bar{t}_{ij}\frac{\partial \tilde{u}_i}{\partial x_j} + \bar{\rho}\in; \qquad \in = \nu\zeta \tag{6}$$

where ν is the kinematic viscosity and ζ is the enstrophy.

Equation (4) was the starting point for deriving an equation for the enthalpy variance and its dissipation rate. The exact equations and examples of how some of the correlations were obtained are given in the Appendix, and the modeled equations are

$$\begin{aligned}
&\frac{\partial}{\partial t}(\rho\tilde{h}''^2/2) + \frac{\partial}{\partial x_j}(\bar{\rho}\tilde{u}_j\tilde{h}''^2/2)\\
&\quad = \frac{\partial}{\partial x_j}\left[\rho(\gamma\alpha + \alpha_t C_{h,2})\frac{\partial(\tilde{h}''^2/2)}{\partial x_j}\right] + 2\mu\gamma\bar{S}_{ij}\left[\frac{\partial}{\partial x_j}(q_{t,i}/\rho)\right.\\
&\quad \left. + \frac{\partial}{\partial x_i}(q_{t,j}/\rho)\right] - \frac{4}{3}\mu\gamma\tilde{S}_{kk}\frac{\partial}{\partial x_j}(q_{t,j}/\rho) - (\gamma - 1)\bar{\rho}\tilde{h}''^2\frac{\partial\tilde{u}_i}{\partial x_i}\\
&\quad - q_{t,i}\frac{\partial\tilde{h}}{\partial x_i} + 2C_{h,4}\gamma\mu\sqrt{\tilde{h}''^2}\zeta - \gamma\bar{\rho}\in_h
\end{aligned} \tag{7}$$

where

$$q_{t,j} = -\bar{\rho}\alpha_t\frac{\partial\tilde{h}}{\partial x_j} \qquad \alpha_t = 0.5[C_h k\tau_h + \nu_t/0.89]$$
$$\tau_h = \tilde{h}''^2/\in_h \qquad \in_h = \alpha\overline{\left(\frac{\partial h''}{\partial x_i}\right)^2} \tag{8}$$

where $\in_h$ is the rate of dissipation of the enthalpy variance, α is the diffusivity, and

$$\nu_t = C_\mu k^2/\nu\zeta \equiv C_\mu k\tau_k$$

is the turbulent kinematic viscosity.

The modeled equation for the dissipation of enthalpy variance is

$$\begin{aligned}
&\frac{\partial}{\partial t}(\bar{\rho}\in_h) + \frac{\partial}{\partial x_j}(\bar{\rho}\tilde{u}_j\in_h) = -\bar{\rho}\in_h\left(C_{h,5}b_{jk} - \frac{\delta_{jk}}{3}\right)\frac{\partial\tilde{u}_j}{\partial x_k}\\
&\quad + C_{h,6}\bar{\rho}k\frac{\partial\sqrt{\tilde{h}''^2}}{\partial x_j}\frac{\partial\tilde{h}}{\partial x_j} + \frac{\partial}{\partial x_j}\left[(\gamma\alpha + C_{h,7}\alpha_t)\frac{\partial\in_h}{\partial x_j}\right]\\
&\quad + C_{h,8}\frac{q_{t,j}}{\tau_h}\frac{\partial h}{\partial x_j} - \gamma\rho\in_h\left[\frac{C_{h,9}}{\tau_h} + \frac{C_{h,10}}{\tau_k}\right]\\
&\quad + C_{h,11}\in_h\left[\frac{\mathrm{D}\bar{\rho}}{\mathrm{D}t} + \frac{\bar{\rho}}{\bar{P}}\max\left(\frac{\mathrm{D}\bar{P}}{\mathrm{D}t}, 0.0\right)\right]
\end{aligned} \tag{9}$$

with

$$b_{ij} = \frac{\tau_{ij}}{\bar{\rho}k} + \frac{2}{3}\delta_{ij}, \qquad \tau_{ij} = -\bar{\rho}\,\widetilde{u_i''u_j''} \tag{10}$$

The constants $\mathrm{C}_h, \ldots \mathrm{C}_{h,11}$ are model constants and are given in Table 1. The turbulent Prandtl number is defined as

$$Pr_t = \nu_t/\alpha_t$$

The choice of α_t merits further elaboration. It was indicated in [6] that experiments in simple shear flows showed that the appropriate timescale for temperature fluctuations is proportional to the arithmetic average of τ_h and τ_k. This is the basis for the modeling indicated in Eq. (8). It should be noted that, traditionally [5,6], the timescale of temperature fluctuations is taken as the geometric average of τ_h and τ_k.

B. Model Constants

When only velocity fluctuations are considered, one of the requirements that model constants must satisfy is deduced by considering the log-law region. In the absence of pressure gradients, the momentum and energy equations in the near wall region reduce to [16]

Table 1 Model constants

C_h	$C_{h,2}$	$C_{h,4}$	$C_{h,5}$	$C_{h,6}$	$C_{h,7}$	$C_{h,8}$	$C_{h,9}$	$C_{h,10}$	$C_{h,11}$
0.0648	0.5	–0.4	–0.05	–0.12	1.45	0.7597	0.87	0.25	0.575

$$\frac{\partial}{\partial x_j}(\bar{t}_{ij} + \tau_{ij}) = 0 \tag{11}$$

and

$$\frac{\partial}{\partial x_j}[-q_{t,j} - q_{\ell,j} + \tilde{u}_i(\bar{t}_{ij} + \tau_{ij})] = 0 \tag{12}$$

where $\bar{t}_{ij}$ and τ_{ij} are the laminar and turbulent stress tensors, and $q_{\ell,j}$ and $q_{t,j}$ are the laminar and turbulent heat flux. Integration of the preceding equations yields

$$(\mu + \mu_t)\frac{\mathrm{d}u}{\mathrm{d}y} = \tau_w \tag{13}$$

and

$$\frac{(\lambda_\ell + \lambda_T)}{C_p}\frac{\mathrm{d}h}{\mathrm{d}y} + u(\mu + \mu_t)\frac{\mathrm{d}u}{\mathrm{d}y} = -q_w \tag{14}$$

where λ is the thermal conductivity and μ is the viscosity.

By eliminating dy from the preceding equations, the following equation is obtained:

$$\frac{\lambda_\ell + \lambda_t}{C_p(\mu + \mu_T)}\frac{\mathrm{d}h}{\mathrm{d}u} + u = -\frac{q_w}{\tau_w} \tag{15a}$$

which reduces to

$$\frac{1}{Pr_t}\frac{\mathrm{d}h}{\mathrm{d}u} + u = -\frac{q_w}{\tau_w} \tag{15b}$$

in the log-law region and

$$\frac{1}{Pr_\ell}\frac{\mathrm{d}h}{\mathrm{d}u} + u = -\frac{q_w}{\tau_w} \tag{15c}$$

in the near wall region, where Pr_ℓ is the laminar Prandtl number. Assuming Pr_t to be constant in the log-law region, Eq. (15b) yields

$$\frac{h}{Pr_t} = -\frac{u^2}{2} - \frac{q_w}{\tau_w}u + \text{const} \tag{16a}$$

and the integral of Eq. (15c) takes the form

$$\frac{h}{Pr_\ell} = -\frac{u^2}{2} - \frac{q_w}{\tau_w}u + \frac{h_w}{Pr_\ell} \tag{16b}$$

Equation (16) illustrates the difference between low- and high-speed flows. For low-speed flows, the dissipation rate in the energy equation is negligible and the temperature has the same dependence on y, the normal distance, as on u. As is seen from Eq. (16), this is not the case for high-speed flows because of the presence of the u^2 term.

Relations involving model constants should, however, be independent of the flow conditions. Although we are dealing with high-speed flow, assuming low-speed conditions in the log-law region makes it possible to derive a relation involving model constants that appear in Eqs. (7) and (9). Proceeding as one normally does when only velocity fluctuations are considered, one can derive the following relation:

$$c_{h,8} = \left[\frac{c_{h,5}c_\mu^{1/2}}{\gamma\kappa} + \frac{c_{h,9}c_h}{\kappa_h c_\mu^{1/2}} + \frac{c_{h,10}c_\mu^{1/2}}{\kappa} - \frac{c_{h,7}\kappa}{\gamma}\right][1 + 0.25c_{h,4}]\frac{c_\mu^{1/2}}{c_h} \tag{17}$$

where κ is the von Karman constant and $\kappa_h = \kappa/Pr_t$.

The value of c_h was chosen based on the work of Launder [17]. As is the case for traditional turbulence models, the remaining coefficients were determined by numerical optimization. As indicated earlier, the flat-plate measurements of [9,10] were used in this work. Because of the high Reynolds numbers, the use of DNS or LES is not a realistic option to model the resulting correlations.

C. Boundary Conditions

The boundary conditions for $\tilde{h}''^2$ and $\in_h$ are discussed next. As may be seen from Eq. (16), $h'' \sim u'' \sim y$. Thus, in the near wall region

$$\tilde{h}''^2 = h_o y^2 + \dots \tag{18}$$

Further, as $y \to 0$, Eq. (7) reduces to

$$\in_h \simeq \frac{\partial}{\partial y}\left[\alpha\frac{\partial\tilde{h}''^2/2}{\partial y}\right] \tag{19}$$

Thus, using Eq. (18), it is seen that $\in_{h,0} = \alpha h_0$. Equation (19) provides the boundary condition for $\in_h$ at the wall.

In the freestream,

$$h + \frac{u^2}{2} = h_\infty + u_\infty^2/2 \tag{20}$$

Setting

$$h = h_\infty + h'', \qquad u = u_\infty + u'' \tag{21}$$

one finds

$$h'' \sim u_\infty u''$$

or

$$\tilde{h}''^2 \sim u_\infty^2 k_\infty \tag{22}$$

k_∞ is determined from the turbulent intensity in the freestream, and thus Eq. (22) provides a value for $\tilde{h}''^2$ at infinity; $\in_h$ at infinity is determined from setting $\alpha_t/\alpha \sim 10^{-2}$.

D. Numerical Procedure

A modification of REACTMB [18], a code that has been developed at North Carolina State University over the last several years, is used to set constants and validate the model. It employs a second-order ENO/TVD upwind method based on the low-diffusion flux-splitting scheme of Edwards [19] to discretize the inviscid fluxes, and central differences are employed for the viscous and diffusion terms. Planar relaxation is used to advance the solution in time.

III. Results and Discussion

A couple of observations should be kept in mind when considering shock-wave/boundary-layer interactions at hypersonic Mach numbers. In the presence of separation, the flow is generally unsteady. Most of the available experimental data are time-averaged data. Yet, none of the three experiments considered here indicated how the data were averaged. Experimental error estimates were indicated in most cases. However, when comparing theory with experiment, one must keep in mind a remark made in [12] to the effect that "no error limits exist for the heat transfer data at Mach numbers greater than 8."

In all of the calculations presented here, a flat-plate calculation was conducted first to match a quantity characteristic of the measured boundary layers. We have chosen to match the displacement thickness δ^* throughout. It should be noted that the resulting boundary-layer flow properties are not necessarily the same for constant (assumed equal to 0.89 throughout) and variable Prandtl number calculations, and as such, different inflow profiles were used to initialize respective calculations of the interactions. Thus, when interpreting results, it is sometimes difficult to determine whether the differences shown are a result of differences in the initial profiles or the model employed or both.

The solutions computed using the model are compared first with the data from the 15-deg ramp experiment of Coleman and Stollery [9]. In this experiment, no flow separation was indicated. The second comparison will be made with the reflected shock experiment of Kussoy and Horstman [11] for a shock angle of 10 deg. In this

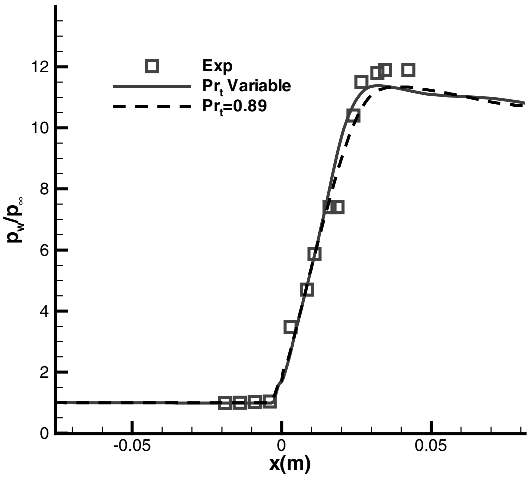

Fig. 1 Computed and measured pressure distribution; 15-deg ramp.

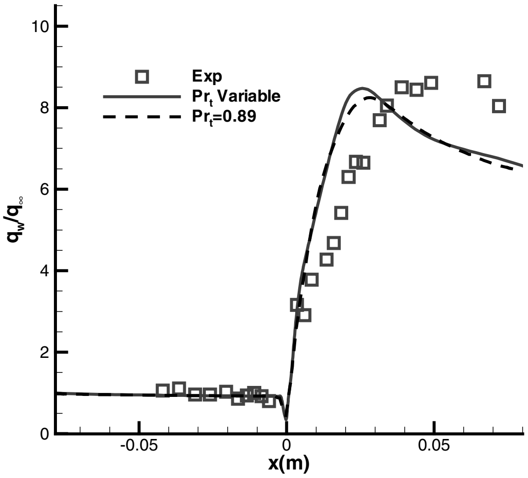

Fig. 2 Computed and measured heat flux; 15-deg ramp.

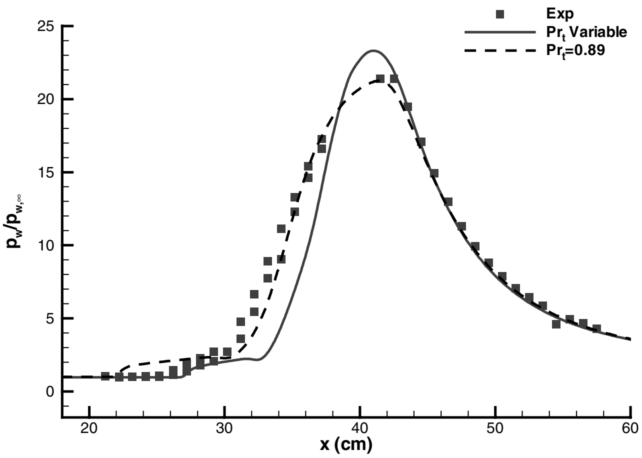

Fig. 4 Computed and measured wall pressure.

experiment, flow separation was indicated. The remaining comparisons will be made with Schülein's two-dimensional flow measurements for shock angles β of 10 and 14 deg. Flow separation was observed for both of these angles.

The freestream conditions for the experiments of Coleman and Stollery [9] are: $M = 9.2$, $Re/L = 47 \times 10^6/\mathrm{m}$, $T_0 = 1070$ K, $T_\infty = 64.5$ K, and $T_w = 295$ K. It has been shown in [15] that use of a 241 × 141 Cartesian grid with constant spacing in the x (flow) direction and geometric spacing in the y (normal) direction resulted in a grid-resolved solution, and this grid is employed in the present calculations. Values of y^+ are less than 0.2. Figures 1 and 2 compare the pressure distributions for constant and variable Prandtl number calculations. As is seen from the figures, the pressure and heat flux distributions are essentially independent of the turbulent Prandtl number. This suggests that the variable Prandtl number calculations have no influence on attached flows. Both calculations underpredict the heat flux in the recovery region. The recovery region has always been difficult to predict using RANS equations. Better results are obtained when a hybrid large eddy simulation/Reynolds-averaged Navier–Stokes (LES/RANS) formulation is employed [20].

The experimental configuration of Kussoy and Horstman [11] is shown in Fig. 3. The conditions for the undisturbed test bed are: $M = 8.18$, $Re/L = 4.9 \times 10^6/\mathrm{ft}$, $T_\infty = 81$ K, $P_\infty = 430$ N/m^2, and a wall temperature of 300 K. In this experiment, flow measurements were provided at a distance of 187 cm from the leading edge of the undisturbed test bed. The wedge was placed later at a distance $X_0 = 124$–140 cm from the plate leading edge. Initial conditions for the flow in the presence of the wedge were obtained by first calculating the flow over the undisturbed flat plate and extracting data from a station 63 cm ahead of the point at which calculations matched the displacement thickness at the 187-cm station.

The largest grid employed in [12] was 160 × 50 in the flow and normal directions. Two grids were employed in this study: 361 × 145 and 481 × 145. The results presented are grid-independent and are for the fine grid. Figures 4 and 5 show a comparison of measured and calculated wall pressure and heat flux. Two sets of heat transfer measurements were provided in [11]: one employing thermocouples and the other Schmidt–Boelter gauges. The uncertainties in surface pressure were estimated to be ±10% or ±80 N/m^2, whichever is larger. Similar uncertainty (i.e., ±10%) was indicated for surface heat transfer measurements. As is seen from Fig. 4, the constant Pr_t number case is characterized by an earlier separation resulting from a slightly stronger incident shock. As a result, the pressure rise resulting from the induced separation shock is in better agreement with the experiment than the variable Pr_t calculation. This is reflected in better heat transfer prediction, indicated in Fig. 5, because wall heat flux scales with pressure for hypersonic Mach numbers. However, the variable Pr_t calculation gives better agreement in regions for which the expansion fan interacts with induced separation and reflected shocks. Figure 6 shows a contour plot of the turbulent Prandtl number. Lower Pr_t numbers result in a lower heat flux to the wall and this is reflected in the wall heat flux in the compression region.

The experimental setup of the Schülein experiment is shown in Fig. 7. A shock generator is mounted on the upper wall, and the resulting oblique shock wave interacts with the turbulent boundary

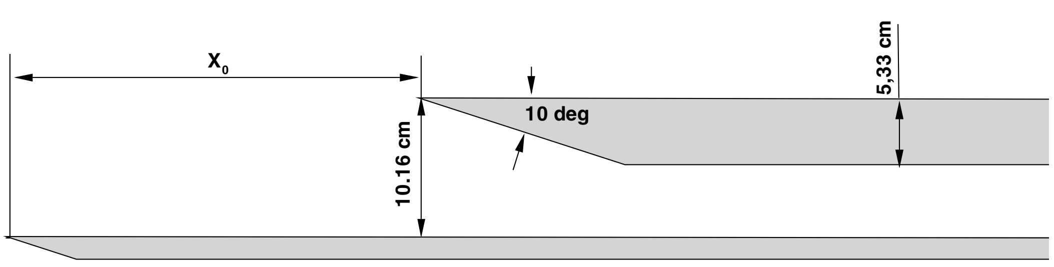

Fig. 3 Experimental configuration of Kussoy et al. [10].

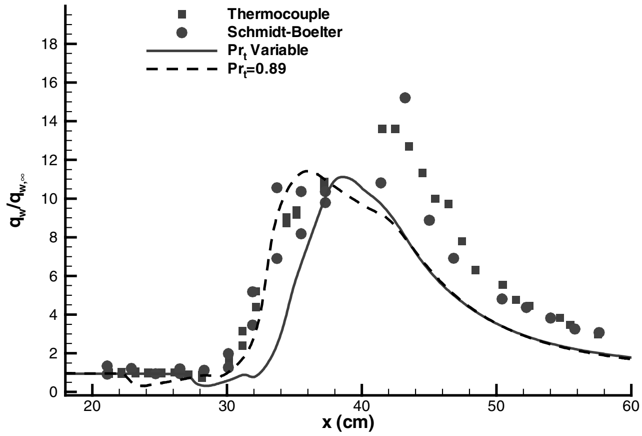

Fig. 5 Computed and measured wall heat flux.

layer growing on the flat plate along the lower wall. The freestream conditions in the test section were $M = 5$, unit $Re = 37 \times 10^6/\text{m}$, $T_0 = 410$ K, $P_0 = 2.12$ MPa, and a wall temperature of 300 ± 5 K. Three grids are used in this investigation: coarse 151×141, medium 243×141, and fine 301×141. Results employing the medium and fine grids gave grid-independent solutions. All results presented next employ the fine grid.

The computational domain for this case is different from that used in the experiment of [12], because the shock generator was further removed from the plate. As a result, there was no need to include the interaction of the expansion fan with the induced separation and reflected shocks. Similar computational domain was used in [21].

It is indicated in [13] that errors in skin friction measurements varied from $\pm 4\%$ in the undisturbed boundary layer to up to 10% at the highest wall shear stress levels. It was further indicated that heat flux measurements compared well with thermocouple-based thin-skin techniques, and the maximum error was $\pm 5\%$.

Figures 8–10 compare predictions of surface pressure, wall shear stress, and wall heat flux, and Figs. 11 and 12 compare temperature and velocity at $x = 376$ mm for $\beta = 10$ deg. It is seen from Figs. 8 and 9 that the results are almost identical for both constant and variable turbulent Prandtl numbers. Both calculations underpredict the pressure in the separated region.

The oil-film interferometry technique cannot be used to determine the extent of the separated region. Instead, conventional oil-film visualization was used to deduce the start and end of the separated region. It is seen from Fig. 9 that the extent of separation is well-predicted. However, some discrepancies are noted in predicting the wall shear stress in the recovery region. The calculations are consistent with the fact that the τ_w should decrease in the constant pressure region. As is seen from Fig. 8, measurements suggest that the pressure is approximately constant after the $x = 370$ mm station.

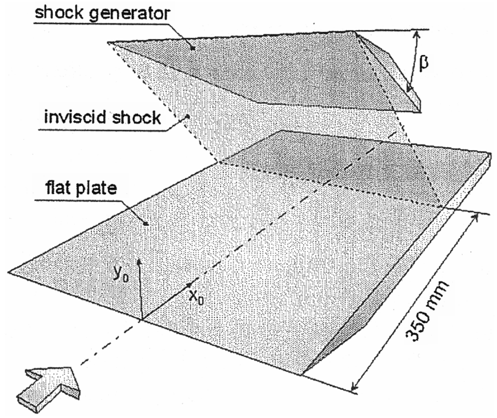

Fig. 7 Schematic of shock-wave/boundary-layer interaction experiment.

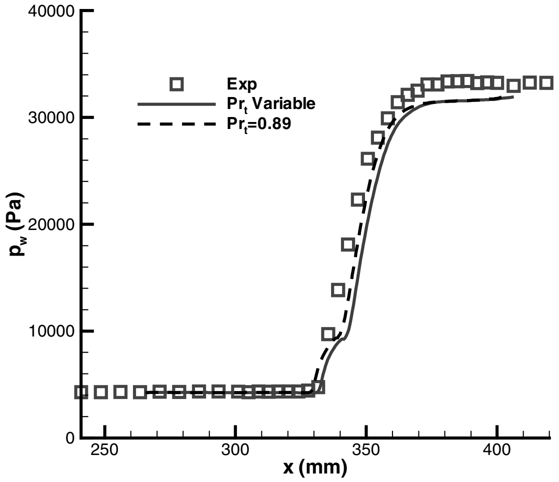

Fig. 8 Computed and measured wall pressure; $\beta = 10$ deg.

It is not clear why the experiment indicates an increase in the wall shear stress downstream of this location. It was pointed out in [21] that skin friction measurements based on velocity measurements (not shown here) are more consistent with what one would expect when the pressure is constant.

Figure 10 shows that the constant Prandtl number calculations overpredict peak heating by a factor of 2. As is seen from the figure, the variable Pr_t results represent a definite improvement over constant Pr_t results. Figures 11 and 12 show that both temperature and velocity profiles at the 376-mm station, which is downstream of

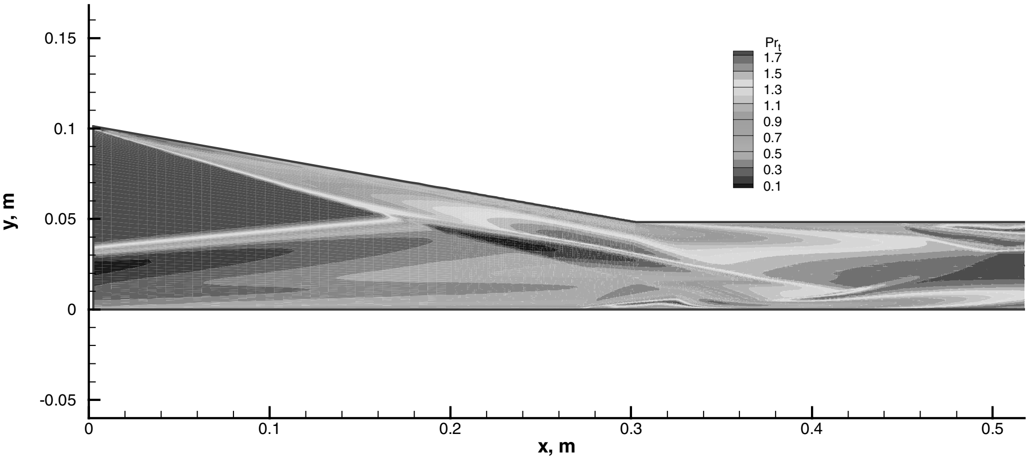

Fig. 6 Prandtl number contours.

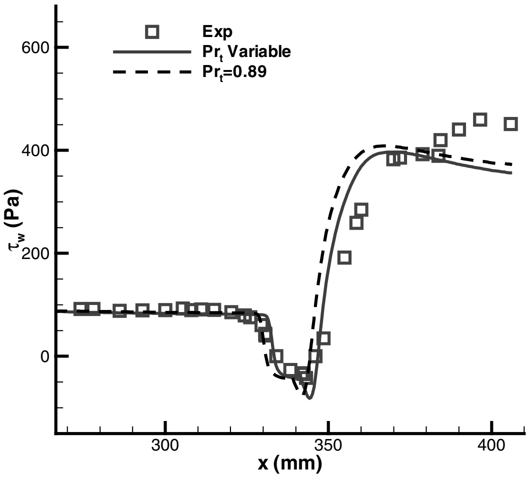

Fig. 9 Computed and measured wall shear stress; $\beta = 10$ deg.

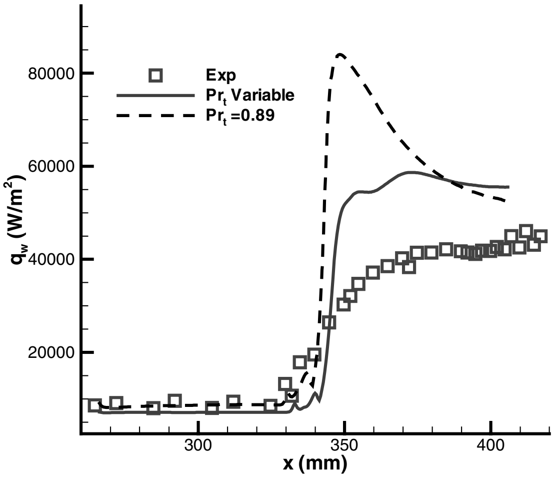

Fig. 10 Computed and measured wall heat flux; $\beta = 10$ deg.

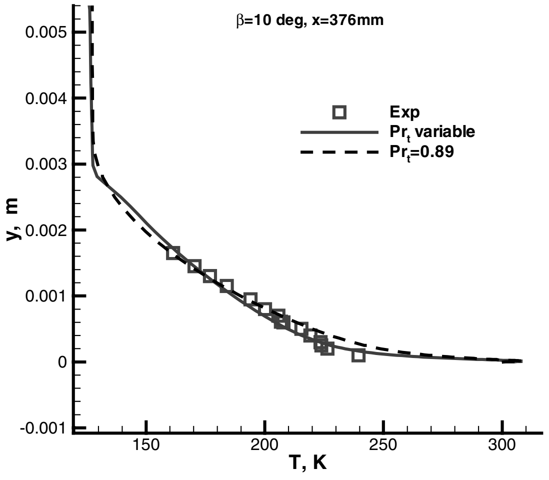

Fig. 11 Computed and measured temperature profile at $x = 376$ mm and $\beta = 10$ deg.

the separation bubble, are in fair-to-good agreement with experiment. As is seen from Fig. 8, the calculated heat flux is about the same for both constant and variable Pr_t at this station. This may explain why the two profiles are essentially independent of Pr_t at this station.

Figure 13 shows a contour plot of Pr_t in the neighborhood of the separated region. In the separated region, Pr_t is about 1.0. As a result, both constant and variable Pr_t solutions yield similar results, as indicated in Fig. 10. Downstream of that region, lower Pr_t values result in increased heat flux away from the wall, and this effect is responsible for the reduction in the wall heat flux compared with the constant Pr_t results. Outside the boundary layer, the first term in the expression for α_t is much less than $\nu_t/0.89$, and thus Pr_t asymptotes to 1.78. This has no real physical significance, because the temperature is essentially constant outside the boundary layer.

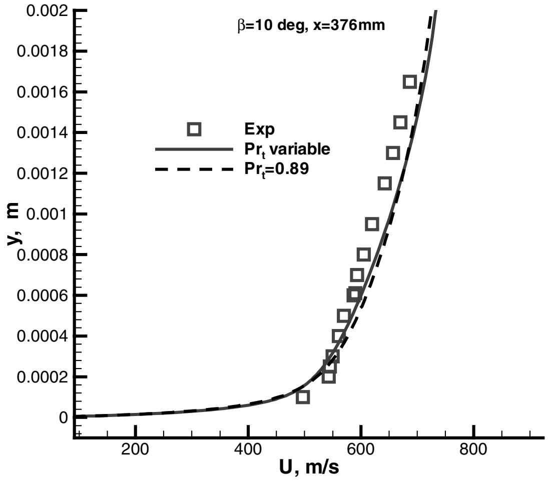

Fig. 12 Computed and measured velocity profile at $x = 376$ mm and $\beta = 10$ deg.

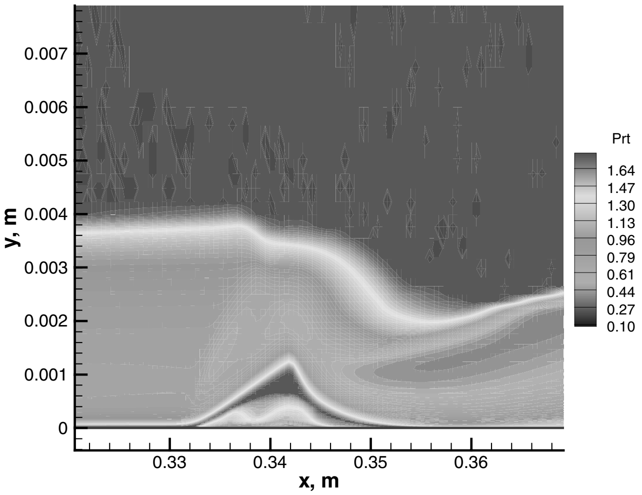

Fig. 13 Prandtl number contours; $\beta = 10$ deg.

Figures 14–19 present similar predictions for the $\beta = 14$ deg case. Similar remarks can be made regarding this case. The only difference is that the separated region is bigger and the heat flux is higher. However, the discrepancies between the predictions and experiment are reduced.

Reference [21] employs the k-ω model. Their results are comparable to those obtained here for the constant Prandtl number. They attribute the discrepancy to the unsteadiness of the flow. However, no time-dependent computations were presented to support their suggestion.

IV. Conclusions

A new approach has been developed for calculating the turbulent Prandtl number as part of the solution. The approach is based on a two-equation model for the enthalpy variance and its dissipation rate. All of the correlations that appear in the exact equations that govern the enthalpy variance and its dissipation rate are modeled to ensure the incorporation of relevant physics into the model equations.

The new formulation is used to study flows characterized by shock-wave/boundary-layer interactions. In general, heat flux

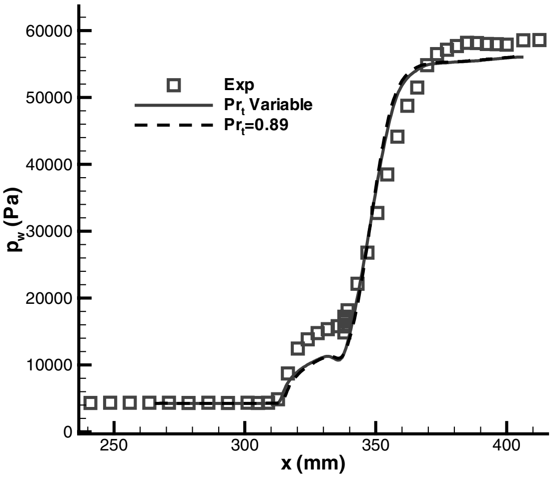

Fig. 14 Computed and measured wall pressure; $\beta = 14$ deg.

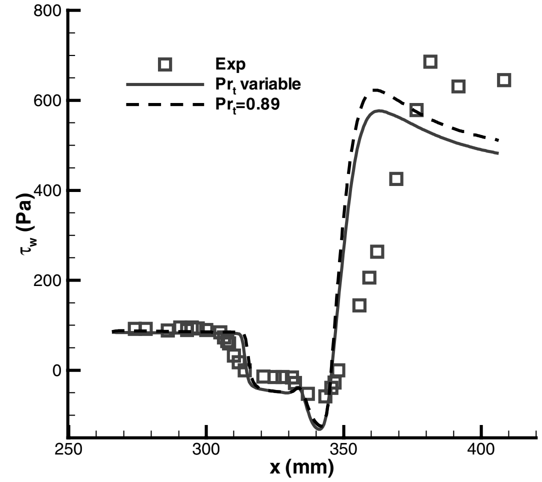

Fig. 15 Computed and measured wall shear stress; $\beta = 14$ deg.

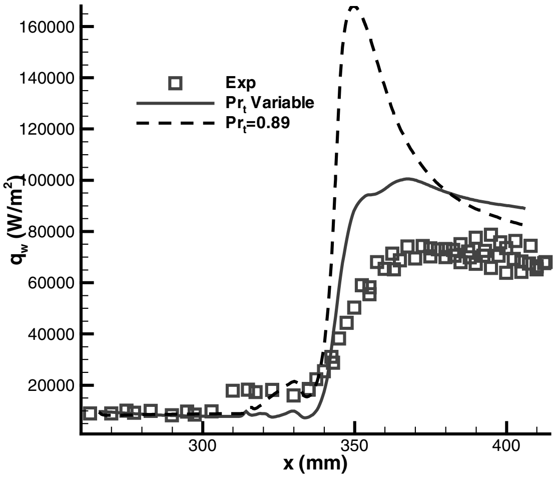

Fig. 16 Computed and measured wall heat flux; $\beta = 14$ deg.

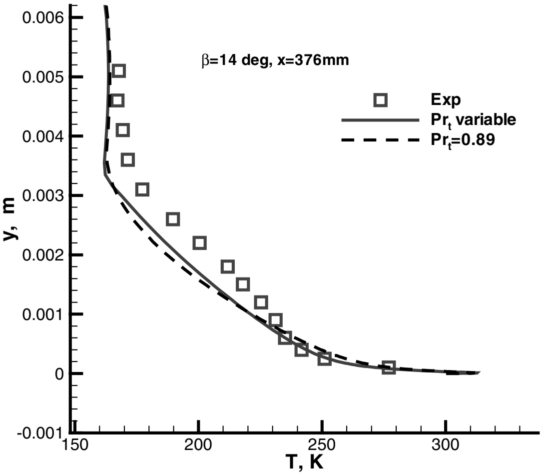

Fig. 17 Computed and measured temperature profile at $x = 376$ mm and $\beta = 14$ deg.

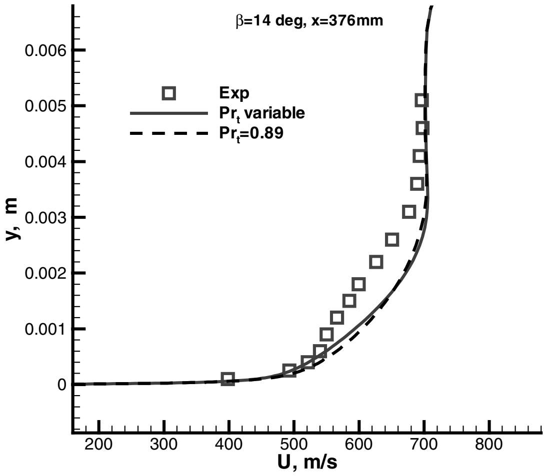

Fig. 18 Computed and measured velocity profile at $x = 376$ mm and $\beta = 14$ deg.

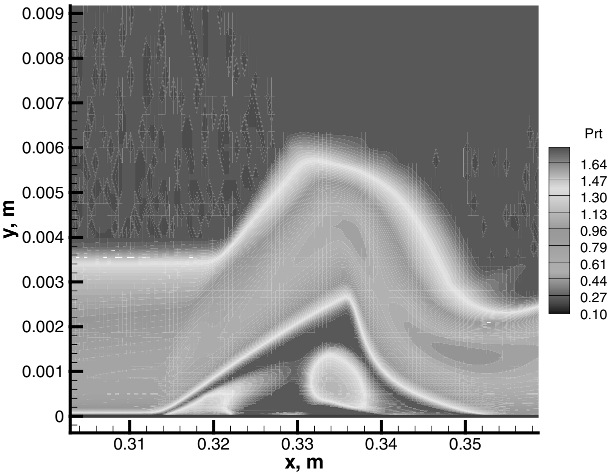

Fig. 19 Contours of turbulent Prandtl number; $\beta = 14$ deg.

calculations showed improvements when considering separated flows. For all cases, surface pressures and wall shear stress were relatively unaffected by the variable Prandtl number formulation.

When comparing pressure, skin friction, and heat flux measurements, the highest errors are associated with heat flux measurements. Despite the discrepancy between computed and measured heat flux, the key to bridging the gap between theory and experiment in flows dominated by shock-wave/boundary-layer interactions is to employ better measurement techniques and use variable turbulent Prandtl number formulations. It has always been difficult for RANS solutions to reproduce the correct flow behavior in the recovery regions. Hybrid LES/RANS approaches have better prediction capabilities and should be used in future investigations.

Appendix A: Enthalpy Variance and Its Dissipation Rate Equations

I. Favre-Averaged Equations

A. *Exact Equations for Enthalpy Variance*

$$\frac{\partial}{\partial t}(\bar{\rho}\tilde{h}''/2) + \frac{\partial}{\partial x_j}[\bar{\rho}\tilde{u}_j\tilde{h}''/2] = -\overline{\rho h'' u_j''}\frac{\partial \tilde{h}}{\partial x_j} - \frac{\partial}{\partial x_j}[\overline{\rho u_j'' h''^2/2}] + \overline{h'' S_h} \tag{A1}$$

where

$$\overline{h'' S_h} = \overline{h''\frac{\mathrm{D}p}{\mathrm{D}t}} - \overline{h''\frac{\partial q_i}{\partial x_i}} + \overline{h''\phi} \tag{A2}$$

B. *Exact Equation for the Dissipation Rate of Enthalpy Variance*

$$\rho\frac{D}{D_t}\varepsilon_h + \overline{2\rho\alpha\frac{\partial h''}{\partial x_j}\frac{\partial h}{\partial x_k}}\frac{\partial \tilde{u}_j}{\partial x_k} + \overline{2\rho\alpha\frac{\partial u_j''}{\partial x_k}\frac{\partial h''}{\partial x_k}}\frac{\partial \tilde{h}}{\partial x_j} + \overline{2\rho\alpha u_j''\frac{\partial h''}{\partial x_k}}\frac{\partial^2 \tilde{h}}{\partial x_j \partial x_k} + \overline{u_j''\frac{\partial}{\partial x_j}\left[\rho\alpha\left(\frac{\partial h''}{\partial x_k}\right)^2\right]} + \overline{2\rho\alpha\frac{\partial u_j''}{\partial x_k}\frac{\partial h''}{\partial x_k}\frac{\partial h''}{\partial x_j}} = \overline{2\rho\alpha\frac{\partial h''}{\partial x_k}\frac{\partial}{\partial x_k}\left[\frac{S_h'}{\rho} - \frac{1}{\rho}\frac{\partial}{\partial x_j}(\overline{\rho u_j'' h''})\right]} \tag{A3}$$

where

$$S_h' = -\frac{\partial q_i}{\partial x_i} + \phi' \tag{A4}$$

II. Modeling Approach

Modeling of the preceding equations was carried out in such a way so as to conform to the following requirements: dimensional and tensorial consistency, Galilean invariance, coordinate-system independence, no wall or damping functions, and use of the gradient diffusion assumption when appropriate. To illustrate, the procedure modeling of a couple of correlations is presented.

A. *Modeling of* $\overline{-h''\frac{\partial q_i}{\partial x_i}}$

$$-h''\frac{\partial q_i}{\partial x_i} = h''\frac{\partial}{\partial x_i}\left(\lambda\frac{\partial T}{\partial x_i}\right) = h''\frac{\partial}{\partial x_i}\left(\rho\alpha\frac{\partial h}{\partial x_i}\right) = \frac{\partial}{\partial x_i}\left[\rho h''\alpha\left(\frac{\partial \tilde{h}}{\partial x_i} + \frac{\partial h''}{\partial x_i}\right)\right] - \rho\alpha\left(\frac{\partial \tilde{h}}{\partial x_i} + \frac{\partial h''}{\partial x_i}\right)\frac{\partial h''}{\partial x_i} - \frac{\partial}{\partial x_i}\left[\rho\alpha h''\frac{\partial \tilde{h}}{\partial x_i} + \rho\alpha\frac{\partial}{\partial x_i}(h''^2/2)\right] - \rho\alpha\frac{\partial \tilde{h}}{\partial x_i}\frac{\partial h''}{\partial x_i} - \rho\alpha\left(\frac{\partial h_i}{\partial x_i}\right)^2 \tag{A5}$$

thus,

$$\overline{-h''\frac{\partial q_i}{\partial x_i}} = \frac{\partial}{\partial x_i}\left[\bar{\rho}\alpha\frac{\partial}{\partial x_i}(\tilde{h}''^2/2)\right] - \rho \in_h \tag{A6}$$

B. *Modeling of* $\overline{\rho\alpha\frac{\partial h''}{\partial x_j}\frac{\partial h}{\partial x_k}}$

$$\rho\alpha\frac{\partial h''}{\partial x_j}\frac{\partial h}{\partial x_k} = \rho\alpha\frac{\partial h''}{\partial x_j}\left(\frac{\partial \tilde{h}}{\partial x_k} + \frac{\partial h''}{\partial x_k}\right) \tag{A7}$$

thus,

$$\overline{\rho\alpha\frac{\partial h''}{\partial x_j}\frac{\partial h}{\partial x_k}} = c_{h,5}\left(b_{jk} + \frac{\delta_{jk}}{3}\right)\in_h \tag{A8}$$

where b_{jk} is the anisotropy tensor, that is,

$$b_{jk} = \frac{\tau_{jk}}{\rho_k} + \frac{2}{3}\delta_{jk}, \qquad \tau_{jk} = -\overline{\rho u_j'' u_k''} \tag{A9}$$

Acknowledgments

The authors would like to acknowledge partial support under NASA Grant NAG1-03030 and U.S. Air Force Contract FA9101-04-C-0015. Moreover, the authors would like to express their appreciation to Erich Schülein for providing us with his measurements.

References

[1] Thivet, F., Knight, D. D., Zheltovodov, A. A., and Maksimov, A. I., “Insights in Turbulence Modeling for Crossing-Shock Wave/Boundary-Layer Interactions,” *AIAA Journal*, Vol. 39, No. 6, 2001, pp. 985–995.

[2] Morkovin, M., “Effects of Compressibility on Turbulent Flows,” *Mecanique de le Turbulence*, edited by A. Favre, Gordon and Breach, New York, 1964, pp. 367–380.

[3] Rizzetta, D. P., Visbal, M. R., and Gastonde, D. V., “Large-Eddy Simulation of Supersonic-Compression Ramp Flow by High-Order Method,” *AIAA Journal*, Vol. 39, No. 12, 2001, pp. 2283–2292.

[4] Boles, J. A., and Edwards, J. R., “Hybrid Large-Eddy/Reynolds-Averaged Navier–Stokes Simulation of a Mach 8.3 Crossing-Shock Interaction,” AIAA Paper 2006-3029, June 2006.

[5] Sommer, T. P., So, R. M. C., and Zhang, H. A., “Near-Wall Variable-Prandtl-Number Turbulence Model for Compressible Flows,” *AIAA Journal*, Vol. 31, No. 1, 1993, pp. 27–35.

[6] Abe, K., Kondoh, T., and Nagano, Y., “A New Turbulence Model for Predicting Flow and Heat Transfer in Separating and Reattaching Flows, 2: Thermal Field Calculations,” *International Journal of Heat and Mass Transfer*, Vol. 38, No. 4, 1995, pp. 1467–1481.

[7] Brinckman, K. W., Kenzakowski, and Dash, S. M., “Progress in Practical Scalar Fluctuation Modeling for High-Speed Aeropropulsive Flows,” AIAA Paper 2005-0508, Jan. 2005.

[8] Robinson, D. F., and Hassan, H. A., “Further Development of the k-ζ (Enstrophy) Turbulence Closure Model,” *AIAA Journal*, Vol. 36, No. 10, 1998, pp. 1825–1833.

[9] Coleman, G. G., and Stollery, J. L., “Heat Transfer from Hypersonic Turbulent Flow at a Wedge Compression Corner,” *Journal of Fluid Mechanics*, Vol. 56, No. 4, 1972, pp. 741–752.

[10] Kussoy, M. I., Horstman, K. C., and Horstman, C. C., “Hypersonic Crossing Shock-Wave/Turbulent Boundary Interactions,” *AIAA Journal*, Vol. 31, No. 12, 1993, pp. 2197–2203.

[11] Kussoy, M. I., and Horstman, K. C., “Documentation of Two- and Three-Dimensional Shock-Wave/Turbulent-Boundary-Layer Interaction Flows at Mach 8.2,” NASA TM 103838, May 1991.

[12] Horstman, C. C., “Hypersonic Shock-Wave Turbulent-Boundary-Layer Interaction Flows-Experiment and Computation,” AIAA Paper 91-1760, June 1991.

[13] Schülein, E., “Optical Skin Friction Measurements in Short-Duration Facilities,” AIAA Paper 2004-2115, June 2004.

[14] Schülein, E., Krogmann, P., and Stanwsky, E., “Documentation of Two-Dimensional Impinging Shock/Turbulent Boundary Layer Interaction Flows,” DLR, German Aerospace Research Center, Paper 1 B 223-96 A 49, Oct. 1996.

[15] Nance, R. P., and Hassan, H. A., “Turbulence Modeling of Shock-Dominated Flow with a *k*-ζ Formulation,” AIAA Paper 99-0153, Jan. 1999.

[16] Wilcox, D. C., *Turbulence Modeling for CFD*, 2nd ed., DCW Industries, La Canada, CA, 1998.

[17] Launder, B. E., “Heat and Mass Transport,” *Turbulent, Topics in Applied Physics*, edited by P. Bradshaw, Springer–Verlag, Berlin, Vol. 12, 1978.

[18] Edwards, J. R., “Advanced Implicit Algorithms for Hydrogen-Air Combustion Calculations,” AIAA Paper 96-3129, June 1991.

[19] Edwards, J. R., “A Low Diffusion Flux Splitting Scheme for Navier–Stokes Calculations,” *Computers and Fluids*, Vol. 26, No. 6, 1997, pp. 635–659.

[20] Xiao, X., Edwards, J. R., and Hassan, H. A., “Blending Functions in Hybrid Large Eddy/Reynolds Averaged Navier–Stokes Simulations,” *AIAA Journal*, Vol. 42, No. 12, 2004, pp. 2508–2515.

[21] Fedorova, N. N., Fedorchenko, I. A., and Schülein, E., “Documentation of Two-Dimensional Impinging Shock/Turbulent Boundary Layer Interaction at M = 5,” *Computational Fluid Dynamics Journal* (Special Issue), Vol. 10, No. 3, 2001, pp. 376–381.

G. Candler
Associate Editor